ACS APPLIED ENERGY MATERIALS
Cite This: ACS Appl. Energy Mater. 2019, 2, 5547−5556
Article
www.acsaem.org

Thienopyrroledione-Based Photosensitizers as Strong Photoinduced Oxidants: Oxidation of $Fe(bpy)_3^{2+}$ in a >1.3 V Dye-Sensitized Solar Cell

Roberta R. Rodrigues, Adithya Peddapuram, Austin L. Dorris, Nathan I. Hammer, and Jared H. Delcamp*

University of Mississippi, Department of Chemistry and Biochemistry, 481 Coulter Hall, University, Mississippi 38677, United States

Supporting Information

ABSTRACT: The design of visible light absorbing organic dyes as strong photoinduced oxidants is needed for many potential applications in energy production and storage. To access more positive potentials, the electron deficient thienopyrroledione building block is promising as a π-bridge combined with weak aryl-ether donor groups and the phenyl-cyanoacetic acid acceptor group. The thienopyrroledione (TPD) building block is compared to the ubiquitous benzothiadiazole (BTD) building block, which was recently used in a dye-sensitized solar cell (DSC) device with >1.4 V photovoltage output. The variation in dye donor group is studied through UV−vis absorption spectroscopy and electrochemical methods both in solution and on TiO_2 films. The TPD building block resulted in a more positive ground state and excited state oxidation potential, a higher photocurrent (up to 3.5 mA/cm^2), and a higher power conversion efficiency (up to 2.9%) than a BTD analogue while retaining comparable photovoltages (~1.3 versus ~1.4 V). Computational analysis was used to better understand the optical properties of the thienopyrroledione-based dyes showing overlap of orbitals at the TPD bridge in the S_0 and S_1 states. The dyes were analyzed in high voltage-DSC devices with a challenging to oxidize redox shuttle, $Fe(bpy)_3^{2+}$, at 1.37 V versus NHE.

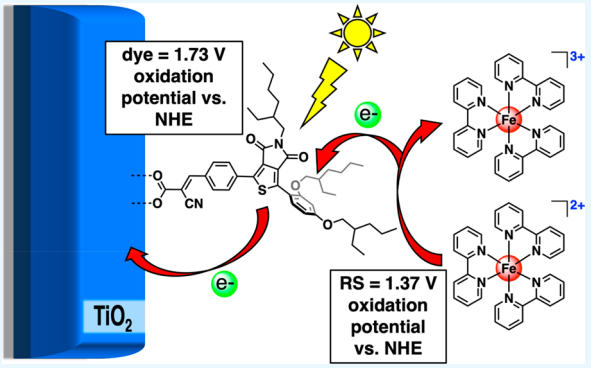

KEYWORDS: *high voltage solar cells, photoinduced oxidant, thienopyrroledione sensitizer, dye-sensitized solar cells, organic sensitizer*

1. INTRODUCTION

Strong photoinduced oxidants are valuable to a range of applications, including solar batteries,[1−3] solar-to-fuel devices,[4−6] solar-to-electric devices,[7−12] and chemical synthesis.[13,14] Generating a photoinduced oxidant via interfacial electron transfer to a semiconductor is attractive for many of these applications since interfacial charge separations are often dramatically longer lived than intramolecular charge transfers (milliseconds versus nanoseconds for many organic dyes).[15−19] Extending charge separation times is attractive for fundamental studies and for practical applications. The study of chromophores bound to metal oxide semiconductors using visible light to generate oxidants <~1.0 V versus NHE are well-known through dye-sensitized solar cell and dye-sensitized photoelectrochemical cell literature;[9,20,21] however, systems significantly more positive in oxidation potential (>1.5 V versus NHE) are less frequently reported.[10,22] Designing chromophores that increase the oxidation potential is an important step toward enabling new visible light driven chemical transformations and using the full potential energy of early visible range photons to give larger potential energy separations of charge which are needed for high-voltage dye-sensitized solar cells (HV DSCs) and multijunction devices, such as sequential series multijunction dye-sensitized solar cells (SSM-DSCs).[10,23−30]

Recently, we reported a >1.4 V HV-DSC device made possible through chromophore design using undoped TiO_2 and $Fe(bpy)_3^{3+/2+}$ as a redox shuttle.[10] While such a high photovoltage from a DSC device is intriguing, the dye used (**RR9**) suffers from the drawbacks of a higher than need excited-state energy, which lowers the photocurrent available from the system (Figure 1). Notably, the use of an aryl-ether-based donor group rather than a commonly employed amine-based donor allowed for the generation of a stronger oxidant upon photoexcitation. The aryl-ether donor with 5 alkyl chains also provided excellent surface protection from back electron transfer events between electrons in TiO_2 and the oxidized redox shuttle, which is commonly referred to as recombination.[31,32] Thus, continued exploration of aryl-ether groups as donors to retain a positive oxidation potential, provide a

Received: April 11, 2019
Accepted: July 8, 2019
Published: July 8, 2019

DOI: 10.1021/acsaem.9b00730
ACS Appl. Energy Mater. 2019, 2, 5547−5556

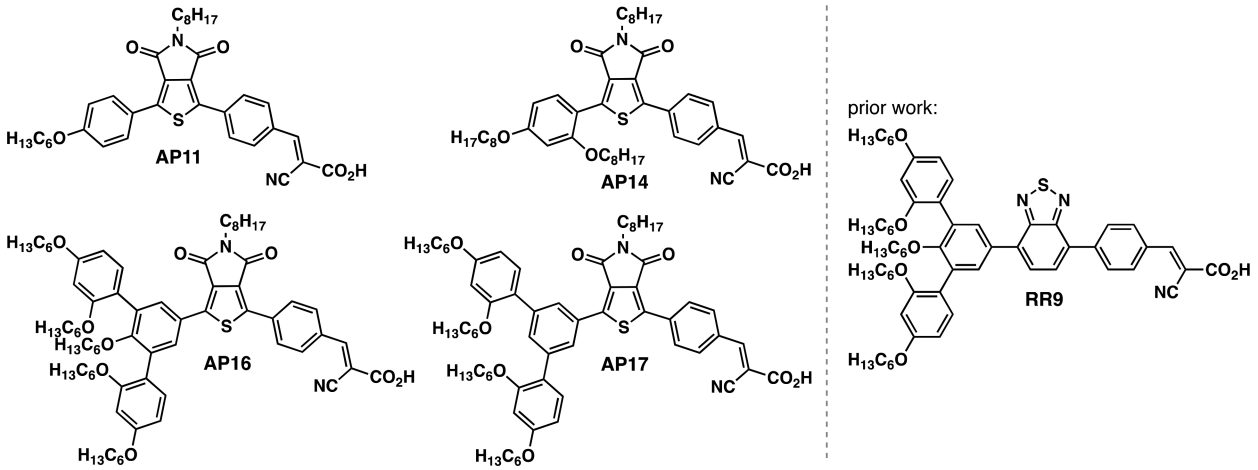

Figure 1. Target structures of **AP11**, **AP14**, **AP16**, and **AP17**. C_6H_{13} refers to an *n*-hexyl substituent and C_8H_{17} refers to 2-ethylhexyl as the substituent.

directional charge transfer event within the dye, and as a platform for alkyl chain incorporation to diminish recombination is desirable. Also, changing of the benzothiadiazole (BTD) to a thienopyrroledione (TPD) allows for the introduction of an alkyl chain on the π-bridge to improve dye solubility and metal oxide surface protection. TPD is well-known in conjugated organic electronic polymer literature as a strongly electron-accepting building block,[33−35] with notable uses in DSC literature, where TPD is combined with aryl amine donors to give broadly absorbing sensitizers.[36−38] In this study, TPD is targeted in place of BTD to lower the excited-state potential energy relative to photoexcited **RR9** leading to less energy loss and potentially a higher photocurrent through a red-shifting of the dye absorption while retaining the strong oxidizing properties of **RR9**$^+$. A series of dyes were selected to probe this possibility using 2-ethylhexyl alkylated TPD with a varying number and location of alkyl ethers on the donor groups (1−5 groups per donor) to probe which donor design is best for recombination resistance (Figure 1).

2. EXPERIMENTAL SECTION

2.1. General Information. Reagents were purchased and used as received without further purification. Thin-layer chromatography (TLC) was conducted with Sorbtech silica XHL TLC plates and visualized with UV light (254 nm). Flash column chromatography was performed with Silicycle ultrapure silica gels P60, 40−63 μm (230−400 mesh) or with a CombiFlash R_f+ instrument using RediSep R_f Gold High Performance HP Silica chromatography prepacked columns. ^{1}H and ^{13}C NMR spectra were recorded on a Bruker Avance-500 (500 MHz) or Bruker Avance-300 (300 MHz) spectrometer. Data reported as s = singlet, d = doublet, t = triplet, q = quartet, p = pentet, m = multiplet, br = broad, ap = apparent, dd = doublet of doublets with coupling constants in Hz, integration. UV−vis spectra were measured with a Cary 5000 spectrometer. All samples were measured in a 1 cm cell at room temperature with dichloromethane as a solvent or on TiO_2 films sensitized with a dye open to air (see SI for the film preparation procedure). Cyclic voltammetry was measured with a C−H Instruments electrochemical analyzer. Voltammetry measurements were carried out in dichloroethane (see SI for dichloromethane measurements) for solution studies using 0.1 M Bu_4NPF_6 as the electrolyte in a three-electrode setup with a glassy carbon working electrode, a silver-wire reference (see SI for Ag/AgCl reference measurements), and a platinum counter electrode with ferrocene as an internal standard. Fc^+/Fc is taken as 0.73 V versus NHE in DCE based on CV comparisons of DCE and DCM (see Figure S2), the reported value of +0.46 versus SCE in DCM,[39] and the reported value of 0.24 V for SCE versus NHE.[40] Voltammetry measurements were conducted at 100 mV/s scan rates. The solution was purged with N_2 prior to measurements and all values are reported versus NHE. For CV measurements on dye-TiO_2 films, the working electrode is an FTO coated glass substrate with 3 μm of 30 nm TiO_2 particles deposited on the conductive side (see SI for the film preparation procedure) and sensitized with a dye as described in the device details section. The solvent used with the film studies is MeCN. HRMS spectra were obtained with a QTOF HRMS utilizing nanospray ionization (ESI). The mass analyzer was set to the 200−2000 Da range. Infrared spectra were recorded with an Agilent Cary 660 ATR-FTIR. For the computational studies, geometries were first energy minimized with MM2 in ChemBio3D Ultra (version 13.0.2.3021). Dihedral angles between benzene rings were set to values between the global minimum and the next local minimum on the conformation energy diagram. Next sequential geometry optimizations were conducted with density functional theory (DFT) using Guassian09 with the B3LYP functional with the following basis sets: first, 3-21G; second, 6-31G(d,p); and finally, 6-311G(d,p). No imaginary frequencies were observed for the optimized geometries. Time-dependent density functional theory (TD-DFT) computations were performed with optimized geometries and with the B3LYP functional and 6-311G(d,p) basis set to compute the 10 lowest energy vertical transitions and oscillator strengths. Orbital images were prepared with Avogadro 1.0.3 with an iso value of 0.02.

2.2. Synthetic Procedures. *4-(5-(2-Ethylhexyl)-3-(4-(hexyloxy)-phenyl)-4,6-dioxo-5,6-dihydro-4H-thieno[3,4-c]pyrrol-1-yl)-benzaldehyde (**3**).* To a flame-dried flask was added 5-(2-ethylhexyl)-4*H*-thieno[3,4-*c*]pyrrole-4,6(5*H*)-dione (**1**) (0.050 g, 0.19 mmol),[41] 1-bromo-4-(hexyloxy)benzene (**A**-Br) (0.048 g, 0.19 mmol), 4-bromobenzaldehyde (**2**) (0.034 g, 0.19 mmol), and toluene (1.88 mL, 0.10 M). The solution was sparged with N_2 for 20 min, and then, $Pd(OAc)_2$ (4.2 mg, 0.019 mmol, 10 mol %), tricyclohexylphosphine (0.010 g, 0.035 mmol, 20 mol %), and Cs_2CO_3 (0.073 g, 0.22 mmol, 1.2 equiv) were added. The mixture was sealed under N_2 and stirred for 16 h at 110 °C. The reaction mixture was extracted with diethyl ether and the organic layer was separated and dried with Na_2SO_4. After removal of the solvent under reduced pressure, the residue was purified via silica gel column with 10% ethyl acetate/hexane as eluent. The product was isolated as a yellow solid (0.019 g, 0.035 mmol, 19% yield). ^{1}H NMR (500 MHz, $CDCl_3$): δ 10.06 (s, 1H), 8.32 (d, J = 8.5 Hz, 2H), 8.11 (d, J = 8.5 Hz, 2H), 7.97 (d, J = 8.0 Hz, 2H), 6.98 (d, J = 9.0 Hz, 2H), 4.03 (t, J = 6.5 Hz, 2H), 3.58 (d, J = 7.0 Hz, 2H), 1.90−1.75 (m, 4H), 1.50−1.40 (m, 2.0H), 1.4−1.1 (m, 11H) 0.92−0.88 (m, 9H) ppm. ^{13}C NMR (125 MHz, $CDCl_3$): δ 191.5, 163.4, 163.3, 161.3, 147.1, 141.3, 136.7, 136.3, 132.4, 130.3, 130.1, 129.2, 128.6, 122.9, 115.0, 68.4, 42.8, 38.4, 31.7, 30.8, 29.9, 29.2, 28.8, 25.8,

DOI: 10.1021/acsaem.9b00730
ACS Appl. Energy Mater. 2019, 2, 5547−5556

24.1, 23.2, 22.7, 14.2, 10.6 ppm. IR (neat): 2924, 2854, 1745, 1698, 1601, 1503, 1462 cm^{-1}. HRMS (ESI-TOF) m/z calcd $[M + Cs]^+$ for $C_{33}H_{39}NO_4SCs$: 678.1655. Found: 678.1659.

*4-(3-(2,4-Bis((2-ethylhexyl)oxy)phenyl)-5-(2-ethylhexyl)-4,6-dioxo-5,6-dihydro-4H-thieno[3,4-c]pyrrol-1-yl)benzaldehyde (**4**).* To a flame-dried flask was added 5-(2-ethylhexyl)-4*H*-thieno[3,4-*c*]pyrrole-4,6(5*H*)-dione (**1**) (0.10 g, 0.38 mmol), 1-bromo-2,4-bis((2-ethylhexyl)oxy)benzene (**B**-Br) (0.16 g, 0.38 mmol),[21] 4-bromobenzaldehyde (**2**) (0.069 g, 0.38 mmol), and toluene (3.8 mL, 0.1 M). The solution was sparged with N_2 for 20 min, and then, $Pd(OAc)_2$ (8.4 mg, 0.038 mmol, 10 mol %), tricyclohexyl phosphine (0.021 g, 0.075 mmol, 20 mol %), and Cs_2CO_3 (0.073 g, 0.45 mmol, 1.2 equiv) were added. The flask was sealed and stirred under N_2 for 16 h at 110 °C. After 16 hours the reaction mixture was extracted with diethyl ether, and the organic layer was separated and dried with Na_2SO_4. After removal of the solvent under reduced pressure, the residue was loaded onto a silica gel column for purification with 10% ethyl acetate/hexane as the eluent. The product was isolated as a yellow solid (0.03 g, 12% yield). ^1H NMR (500 MHz, $CDCl_3$): δ 10.05 (s, 1H), 8.56 (d, J = 9.0 Hz, 1H), 8.30 (d, J = 8.5 Hz, 2H), 7.96 (d, J = 8.0 Hz, 2H), 6.65 (dd, J = 11, 2.0 Hz, 1H), 6.54 (d, J = 2.0 Hz, 1H), 4.02 (d, J = 5.5, 2H), 3.92−3.90 (m, 2H), 3.57 (d, J = 7.5 Hz, 2H), 1.90−1.7.0 (m, 2H), 1.70−1.55 (m, 1.0) 1.76−1.25 (m, 24H), 0.98−0.87 (m, 18H) ppm. ^{13}C NMR (125 MHz, $CDCl_3$): δ 191.6, 163.8, 163.6, 162.7, 157.5, 143.5, 141.6, 137.0, 136.4, 132.9, 130.8, 130.3, 130.1, 128.5, 112.3, 105.5, 99.5, 71.8, 70.8, 42.7, 39.7, 39.5, 38.4, 31.0, 30.8, 30.6, 29.9, 29.3, 29.2, 28.8, 24.2, 24.1, 24.0, 23.3, 23.2, 23.2, 14.2, 14.2, 11.4, 11.3, 10.6 ppm. IR (neat): 2923, 2856, 1742, 1689, 1599, 1568, 1460 cm^{-1}. HRMS (ESI-TOF) m/z calcd $[M + Cs]^+$ for $C_{43}H_{59}NO_5SCs$: 834.3168. Found: 834.3143 with an identical isotope pattern to the predicted pattern.

*4-(5-(2-Ethylhexyl)-4,6-dioxo-3-(2,2′,2″,4,4″-pentakis(hexyloxy)-[1,1′:3′,1″-terphenyl]-5′-yl)-5,6-dihydro-4H-thieno[3,4-c]pyrrol-1-yl)benzaldehyde (**5**).* To a flame-dried flask was added 5-(2-ethylhexyl)-4*H*-thieno[3,4-*c*]pyrrole-4,6(5*H*)-dione (**1**) (0.10 g, 0.38 mmol), 5′-bromo-2,2′,2″,4,4″-pentakis(hexyloxy)-1,1′:3′,1″-terphenyl (**5**) (0.30 g, 0.38 mmol),[10] 4-bromobenzaldehyde (**2**) (0.069 g, 0.38 mmol), and toluene (3.7 mL, 0.1 M). The solution was sparged with N_2 for 20 min, then $Pd(OAc)_2$ (8.4 mg, 0.038 mmol, 10 mol %), tricyclohexyl phosphine (10.6 mg, 0.075 mmol, 20 mol %), and Cs_2CO_3 (0.073 mg, 0.22 mmol, 1.2 equiv) were added. The vessel was sealed and stirred under N_2 for 16 h at 110 °C. After 16 hours, the reaction mixture was extracted with diethyl ether, and the organic layer was separated and dried with Na_2SO_4. After removal of the solvent under reduced pressure, the residue was loaded onto a silica gel column for purification with 5−10% ethyl acetate/hexane as eluent. The product was isolated as a yellow solid (0.05 g, 0.046 mmol, 12% yield). ^1H NMR (500 MHz, $CDCl_3$): δ 10.05 (s, 1H), 8.31 (d, J = 8.0 Hz, 2H), 8.04 (s, 2H), 7.96 (d, J = 8.0 Hz, 2H), 7.30 (d, J = 8.5 Hz, 2H), 6.55−6.52 (m, 4H), 4.00 (t, J = 6.0 Hz, 4H), 3.96 (t, J = 6.5 Hz, 4H), 3.56 (d, J = 7.0 Hz, 2H), 3.25 (t, J = 6.0 Hz, 2H), 1.90−1.75 (m, 6H), 1.75−1.63 (m, 5H), 1.63−1.54 (m, 4H), 1.54−1.41 (m, 5H), 1.41−1.11 (m, 25H), 1.10−1.00 (m, 4H), 1.00−0.80 (m, 12H), 0.80−0.65 (m, 9H). ^{13}C NMR (125 MHz, $CDCl_3$): δ 191.6, 163.4, 163.0, 160.0, 158.3, 157.5, 147.7, 141.5, 136.6, 136.5, 133.0, 132.4, 132.2, 131.2, 130.3, 129.5, 128.6, 124.4, 120.2, 104.9, 100.2, 72.9, 68.6, 68.2, 42.8, 38.2, 31.8, 31.8, 31.7, 31.6, 30.7, 30.0, 29.9, 29.5, 29.3, 28.7, 25.9, 25.9, 25.5, 24.0, 23.2, 22.8, 22.7, 14.2, 14.2, 14.2, 10.6 ppm. IR (neat): 2926, 2859, 1748, 1698, 1605, 1504 cm^{-1}. MS (ESI-TOF) m/z calcd $[M+Cs]^+$ for $C_{69}H_{95}NO_8SCs$ $[M + Cs]^+$: 1230.5833. Found: 1230.5850 with an identical isotope pattern to the predicted pattern.

*4-(5-(2-Ethylhexyl)-4,6-dioxo-3-(2,2″,4,4″-tetrakis(hexyloxy)-[1,1′:3′,1″-terphenyl]-5′-yl)-5,6-dihydro-4H-thieno[3,4-c]pyrrol-1-yl)benzaldehyde (**6**).* To a flame-dried flask were added 4-(5-(2-ethylhexyl)-4,6-dioxo-5,6-dihydro-4*H*-thieno[3,4-*c*]pyrrol-1-yl)-benzaldehyde (**7**) (0.100 g, 0.27 mmol, 5′-chloro-2,2″,4,4″-tetrakis-(hexyloxy)-1,1′:3′,1″-terphenyl (**D**-Cl) (0.197 g, 0.29 mmol), and toluene (2.7 mL, 0.1 M). The solution was purged with N_2 for 20 min. Then, $Pd(OAc)_2$ (3.0 mg, 0.0135 mmol, 5 mol %), tricyclohexyl phosphine (7.6 mg, 0.0268 mmol, 10 mol %), and Cs_2CO_3 (0.105 g, 0.32 mmol) were added. The reaction was sealed under N_2 and stirred for 16 h at 110 °C. After 16 h, the reaction mixture was extracted with diethyl ether and the organic layer was separated and dried with Na_2SO_4. After removal of the solvent under reduced pressure, the residue was loaded onto a silica gel column for purification with 5−10% ethyl acetate/hexane as eluent. The product was isolated as a yellow solid (0.100 g, 0.100 mmol, 37% yield). ^1H NMR (500 MHz, $CDCl_3$): δ 10.06 (s, 1H), 8.33 (d, J = 8.0 Hz, 2H), 8.23 (s, 2H), 7.98 (d, J = 7.5 Hz, 2H), 7.84 (s, 1H), 7.40 (d, 8.50, 2H), 6.59−6.57 (m, 4H), 4.02−3.95 (m, 8H), 3.59 (d, J = 7 Hz, 2H), 1.92−1.77 (m, 4H), 1.77−1.65 (m, 4H), 1.60−1.41 (m, 6H), 1.41−1.3 (m, 24H), 1.00−0.80 (m, 12H), 0.80−0.75 (m, 9H), ppm. ^{13}C NMR (125 MHz, $CDCl_3$): δ = 191.4, 163.3, 162.8, 160.1, 157.1, 147.8, 142.0, 138.9, 136.6, 136.3, 133.0, 132.3, 131.3, 130.2, 130.2, 129.2, 128.5 127.3, 122.6, 105.5, 100.4, 68.4, 68.2, 42.7, 38.2, 31.7, 31.7, 30.6, 29.3, 29.2, 28.6, 26.0, 25.8, 23.9, 23.1, 22.6, 22.5, 14.1, 14.1, 14.0, 10.5 ppm. IR (neat): 2920, 2852, 1701, 1606 cm^{-1}. MS (ESI-TOF) m/z calcd $[M]^+$ for $C_{36}H_{83}NO_7S$: 997.6. Found: 998.0 with an identical isotope pattern to the predicted pattern.

*4-(5-(2-Ethylhexyl)-4,6-dioxo-5,6-dihydro-4H-thieno[3,4-c]-pyrrol-1-yl)benzaldehyde (**7**).* To a flame-dried flask was added 5-(2-ethylhexyl)-4*H*-thieno[3,4-*c*]pyrrole-4,6(5*H*)-dione (**1**) (0.40 g, 1.51 mmol), 4-bromobenzaldehyde (**2**) (0.28 g, 1.50 mmol), and toluene (15 mL, 0.1M). The solution was sparged with N_2 for 20 min, and then, $Pd(OAc)_2$ (17 mg, 0.076 mmol 5 mol %), tricyclohexyl phosphine (0.042 g, 0.15 mmol, 10 mol %), and Cs_2CO_3 (0.58 g, 1.8 mmol, 1.2 equiv) were added. The vessel was sealed under N_2 and stirred for 4 h at 110 °C. After 4 h, the reaction mixture was extracted with diethyl ether and the organic layer was separated and dried with Na_2SO_4. After removal of the solvent under reduced pressure, the residue was loaded onto a silica gel column for purification with 10−20% ethyl acetate/hexane as eluent. The product was isolated as a pale-yellow solid (200 mg, 0.542 mmol, 36% yield). ^1H NMR (500 MHz, $CDCl_3$): δ 10.06 (s, 1H), 8.30 (d, J = 8.5 Hz, 2H), 7.97 (d, J = 8.0 Hz, 2H), 7.82 (s, 1H), 3.56 (d, J = 7.0 Hz, 2H), 1.84−1.81 (m, 1H), 1.35−1.25 (m, 8H), 0.97−0.82 (m, 6H) ppm. ^{13}C NMR (125 MHz, $CDCl_3$): δ 191.4, 163.4, 162.7, 145.5, 138.4, 137.0, 136.2, 131.0, 130.4, 128.6, 124.7, 42.8, 38.4, 30.7, 28.7, 24.0, 23.2, 14.2, 10.6 ppm. IR (neat): 3088, 2954, 2925, 2857, 1757, 1694, 1601, 1532 cm^{-1}. MS (ESI-TOF) m/z calcd $[M + Cs]^+$ for $C_{21}H_{23}NO_3SCs$: 502.0. Found: 502.0 with an identical isotope pattern to the predicted pattern.

*5′-Chloro-2,2″,4,4″-tetrakis(hexyloxy)-1,1′:3′,1″-terphenyl (**D**-Cl).* To a flame-dried flask was added commercially available 1,3-dibromo-5-chlorobenzene (**8**) (1.5 g, 5.5 mmol), (2,4-bis(hexyloxy)-phenyl)boronic acid (**9**) (3.9 g, 12.2 mmol),[42] toluene (22 mL, 0.25 M), and aqueous K_2CO_3 (2.7 mL of a 2.0 M solution). The solution was sparged with N_2 for 20 min, then $Pd(PPh_3)_4$ (64 mg, 0.55 mmol, 10 mol %) was added. The reaction was stirred under N_2 for 16 h at 110 °C. After 16 hours, the reaction mixture was extracted with diethyl ether, and the organic layer was separated and dried with Na_2SO_4. After removal of the solvent under reduced pressure, the residue was loaded into a silica gel column for purification with 2−5% diethyl ether/hexane as eluent. The product was isolated as a colorless oil (1.37 g, 2.2 mmol, 41% yield). ^1H NMR (500 MHz, $CDCl_3$): δ 7.53 (s, 1H), 7.47 (d, J = 1.5 Hz, 2H), 7.26 (d, J = 8.0 Hz, 2H), 6.54−6.53 (m, 4H), 3.98 (t, J = 6.5 Hz, 4H), 3.95 (t, J = 6.5 Hz, 6H) 1.85−1.75 (m, 4H), 1.75−1.67 (m, 4H), 1.52−1.44 (m, 4H), 1.44−1.38 (m, 4H), 1.38−1.30 (m, 8H), 1.30−1.18 (m, 8H), 0.92 (t, J = 7.0 Hz, 6H), 0.85 (t, J = 7.0 Hz, 6H) ppm. ^{13}C NMR (125 MHz, $CDCl_3$): δ 160.1, 157.1, 139.6, 132.9, 131.2, 128.6, 127.5, 122.4, 105.4, 100.4, 68.5, 68.2, 31.8, 31.7, 29.4, 29.3, 26.1, 25.9, 22.8, 22.7, 14.2, 14.2 ppm. IR (neat): 2925, 2859, 1605, 1578, 1505 cm^{-1}. HRMS (ESI-TOF) m/z calcd $[M + Cs]^+$ for $C_{42}H_{61}ClO_4Cs$: 797.3313. Found: 797.3297 with an identical isotope pattern to the predicted pattern.

*(E)-2-Cyano-3-(4-(5-(2-ethylhexyl)-3-(4-(hexyloxy)phenyl)-4,6-dioxo-5,6-dihydro-4H-thieno[3,4-c]pyrrol-1-yl)phenyl)acrylic Acid (**AP11**).* To a round-bottom flask was added 4-(5-hexyl-3-(4-(hexyloxy)phenyl)-4,6-dioxo-5,6-dihydro-4H-thieno[3,4-*c*]pyrrol-1-

DOI: 10.1021/acsaem.9b00730
ACS Appl. Energy Mater. 2019, 2, 5547−5556

Scheme 1. Synthetic Route to Target Dyes AP11, AP14, AP16, and AP17

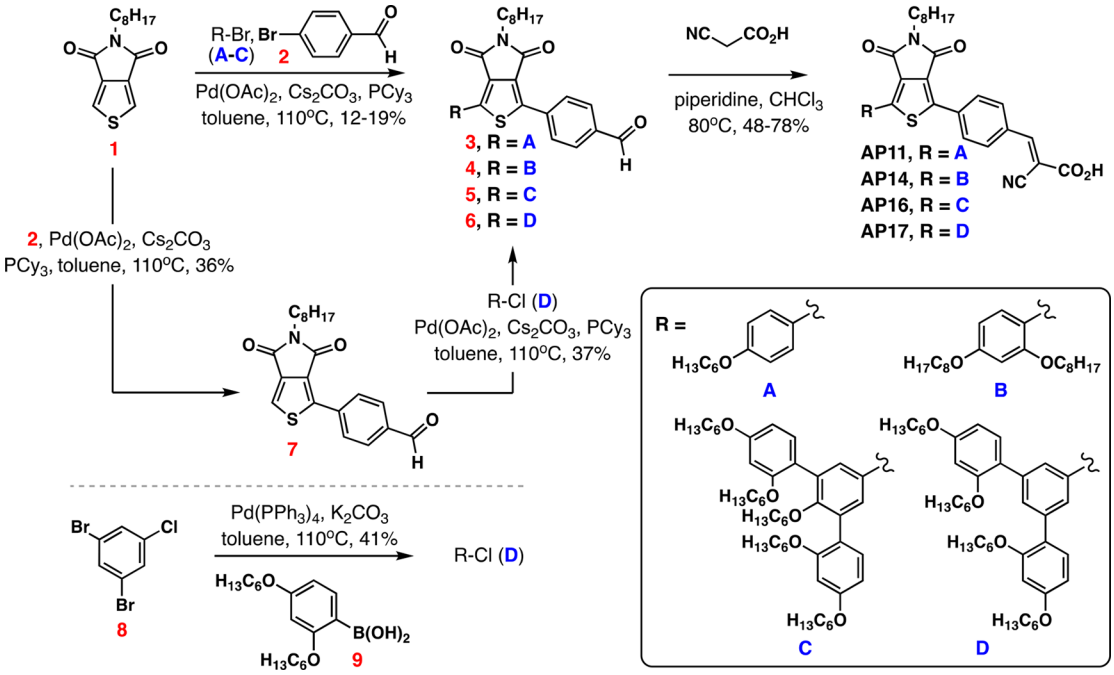

yl)benzaldehyde (**3**) (26 mg, 0.047 mmol) and $CHCl_3$ (4.7 mL, 0.01 M), cyanoacetic acid (18 mg, 0.141 mmol) and piperidine (0.033 mL, 0.329 mmol). The flask was sealed under N_2 and stirred at 80 °C for 16 h. The reaction mixture was acidified with acetic acid (~1.0 mL), and then, it was extracted with diethyl ether and water. The organic layer was separated, and the solvent was evaporated under reduced pressure. The yellow solid was purified through a silica gel column with a mixture of 5−10% methanol: dichloromethane, and the organic layer was concentrated under reduced pressure to give the product as a yellow solid (17 mg, 0.028 mmol, 59%). ^{1}H NMR (500 MHz, DMSO-d_6 at 50 °C): δ 8.26 (d, J = 8.5 Hz, 2H), 8.11 (d, J = 8.0 Hz, 3H), 8.06 (d, J = 8.0 Hz, 2H), 7.10 (d, J = 8.5 Hz, 2H), 4.08 (t, J = 6.0 Hz, 2H), 3.48 (d, J = 5.5 Hz, 2H), 1.82−1.69 (m, 4H), 1.51−1.37 (m, 3.0H), 1.37−1.10 (m, 10H), 0.89 (t, J = 5.5 Hz, 9H) ppm. ^{13}C NMR data is not available due to limited solubility of the compound. IR (neat): 3480, 2922, 2855, 1741, 1691, 1596, 1503 cm^{-1}. MS (ESI-TOF) m/z calcd $[M - H]^-$ for $C_{36}H_{39}N_2O_5S$: 611.3. Found: 611.3 with an identical isotope pattern to the predicted pattern.

*(E)-3-(4-(3-(2,4-Bis((2-ethylhexyl)oxy)phenyl)-5-(2-ethylhexyl)-4,6-dioxo-5,6-dihydro-4H-thieno[3,4-c]pyrrol-1-yl)phenyl)-2-cyanoacrylic Acid (**AP14**).* To a round-bottom flask was added 4-(5-(2-ethylhexyl)-3-(4-((2-ethylhexyl)oxy)-2-(octan-3-yloxy)phenyl)-4,6-dioxo-5,6-dihydro-4H-thieno[3,4-c]pyrrol-1-yl)benzaldehyde (**4**) (45 mg, 0.064 mmol), $CHCl_3$ (6.4 mL, 0.01 M), cyanoacetic acid (16.3 mg, 0.192 mmol), and piperidine (0.044 mL, 0.448 mmol). The flask was sealed under N_2 and stirred at 80 °C for 16 h. The reaction mixture was acidified with acetic acid and then extracted with diethyl ether and water. The organic layer was separated, and the solvent was evaporated under reduced pressure. The organic layer was purified through a silica gel column with a mixture of 5−10% methanol: dichloromethane. The organic layer was concentrated under reduced pressure to give the product as a yellow solid (20 mg, 0.026 mmol, 48%). ^{1}H NMR (500 MHz, $CDCl_3$): δ 8.55 (d, J = 8.5 Hz, 1H), 8.36−8.22 (m, 3H), 8.10 (d, J = 7.5 Hz, 2H), 6.64 (d, J = 10.5 Hz, 2H), 6.54 (s, 1H), 4.02 (d, J = 4.5 Hz, 2H), 3.96−3.85 (m, 2H), 3.56 (d, J = 7 Hz, 2H), 1.97−1.69 (m, 8H), 1.79−1.38 (m, 8H), 1.38−1.28 (m, 11H), 1.00−0.79 (m, 18H) ppm. ^{13}C NMR data is not available due to limited solubility of the compound. IR (neat): 2957, 2922, 2854, 1740, 1689, 1568 cm^{-1}. MS (ESI-TOF) m/z calcd $[M - H]^-$ for $C_{46}H_{59}N_2O_6S$: 767.4. Found: 767.5 with an identical isotope pattern to the predicted pattern.

*(E)-2-Cyano-3-(4-(5-(2-ethylhexyl)-4,6-dioxo-3-(2,2′,2″,4,4″-pentakis(hexyloxy)-[1,1′:3′,1″-terphenyl]-5′-yl)-5,6-dihydro-4H-thieno[3,4-c]pyrrol-1-yl)phenyl)acrylic Acid (**AP16**).* To a round-bottom flask was added **5** (100 mg, 0.091 mmol), chloroform (9.1 mL, 0.01M), cyanoacetic acid (23 mg, 0.27 mmol), and piperidine (0.063 mL, 0.64 mmol). The flask was sealed under N_2 and stirred at 80 °C for 16 h. Then acetic acid (1.0 mL) was added, and the mixture was extracted with diethyl ether and water. The organic layer was purified through a silica gel column with a mixture of 5−10% methanol: dichloromethane. The organic layer was concentrated under reduced pressure to give the product as an orange solid (30 mg, 0.026 mmol, 57%). ^{1}H NMR (300 MHz, DMSO-d_6 at 100 °C): δ 8.27 (d, J = 8.4 Hz, 2H), 8.17 (s, 2H), 8.10 (d, J = 8.4, 2H), 7.98 (s, 2H), 7.21 (d, J = 8.4, 2H), 6.65 (d, J = 1.8, 2H), 6.58 (dd, J = 10.5 Hz, J = 2.1 Hz, 2H), 4.16−3.98 (m, 8H), 3.45 (d, J = 6.9 Hz, 2H), 3.19 (t, J = 6.3 Hz, 2H), 1.80−1.66 (m, 5H), 1.66−1.51 (m, 5H), 1.51−1.38 (m, 5H), 1.38−0.95 (m, 34H), 0.95−0.78 (m, 12), 0.78−0.60 (m, 9H) ppm. ^{13}C NMR data is not available due to limited solubility of the compound. IR (neat): 2925, 2858, 1744, 1696, 1601, 1504 cm^{-1}. MS (ESI-TOF) m/z calcd $[M - H]^-$ for $C_{72}H_{95}N_2O_9S$: 1163.7. Found: 1163.6 with an identical isotope pattern to the predicted pattern.

*(E)-2-Cyano-3-(4-(5-(2-ethylhexyl)-4,6-dioxo-3-(2,2″,4,4″-tetrakis(hexyloxy)-[1,1′:3′,1″-terphenyl]-5′-yl)-5,6-dihydro-4H-thieno[3,4-c]pyrrol-1-yl)phenyl)acrylic Acid (**AP17**).* To a round-bottom flask was added 4-(5-(2-ethylhexyl)-4,6-dioxo-3-(2,2″,4,4″-tetrakis(hexyloxy)-[1,1′:3′,1″-terphenyl]-5′-yl)-5,6-dihydro-4H-thieno[3,4-c]pyrrol-1-yl)benzaldehyde (**6**) (50 mg, 0.05 mmol), chloroform (5.0 mL, 0.01 M), cyanoacetic acid (12 mg, 0.12 mmol), and piperidine (0.034 mL, 0.35 mmol) into the flask. The flask was sealed under N_2 and stirred at 80 °C for 16 h. Then acetic acid (1.0 mL) was added, and mixture was extracted with diethyl ether and water. The organic layer was purified through a silica gel column with mixture of 5−10% methanol: dichloromethane. The organic layer was concentrated under reduced pressure to give an orange product (40 mg, 0.037 mmol, 78%). ^{1}H NMR (500 MHz, DMSO-d_6 at 100 °C): δ 8.28 (d, J = 7.0 Hz, 2H), 8.22 (s, 1H), 8.18 (s, 2H), 8.09 (d, J = 7.5 Hz, 2H), 7.74 (s, 1H), 7.36 (d, J = 8.0 Hz, 2H), 6.72−6.55 (m, 4H), 4.05 (t, J = 6.5, 4H), 4.01 (t, J = 6.0, 4H), 3.52 (d, J = 6.5 Hz, 2H), 1.85−1.70 (m, 5H), 1.70−1.54 (m, 5H), 1.54−1.39 (m, 5H), 1.49−0.97 (m, 37H), 0.97−0.74 (m, 12H), 0.71 (t, J = 7.5 Hz, 6H) ppm. IR (neat): 2922, 2853, 1697, 1601, 1504

DOI: 10.1021/acsaem.9b00730
ACS Appl. Energy Mater. 2019, 2, 5547−5556

cm^{-1}. HRMS (ESI-TOF) m/z calcd $[M - H]^-$ for $C_{66}H_{84}N_2O_8S$: 1063.5870. Found: 1063.5900 with an identical isotope pattern to the predicted pattern.

3. RESULTS AND DISCUSSION

3.1. Synthesis. The synthesis of the target dyes **AP11**, **AP14**, **AP16**, and **AP17** began with either the palladium catalyzed single or double C−H activation of starting TPD building block **1** (Scheme 1).[41] A double C−H activation route was used to install the known bromine substituted aryl ether donor groups (**A**−**C**)[10,21] and 4-bromobenzaldehyde (**2**) in one pot for rapid access to aryl ether donor-TPD-Ph-COH intermediates **3**−**5** in route to **AP11**, **AP14**, and **AP16**. The aryl-ether group (**D**-Cl) used with **AP17** was most readily accessed as the chlorine substituted coupling partner from commercial materials in one step from 1,3-dibromo-5-chlorobenzene (**8**) and dialkoxyphenyl boronic acid **9**.[42] A two-step sequential C−H activation route was used to couple aryl ether **D**-Cl to TPD by first synthesizing TPD-Ph-COH (**7**) via C−H activation from TPD **1** and **2** in 36% yield followed by coupling of **D**-Cl with **7** in 37% yield to give **6**. Knoevenagel condensation with intermediates **3**−**6** and cyanoacetic acid awarded the target dyes in 48−78% yield.

3.2. Optical Properties. The optical properties of the dyes were examined both in solution and on TiO_2 through UV−vis absorption spectroscopy to compare the effect of varying the number and position of the alkoxy-ether groups. In dichloromethane, the lowest energy absorption feature presented as a shoulder in the spectrum for each of the dyes at about 405−440 nm with absorption curve onsets in the following order from shortest to longest wavelength: **AP17** < **AP16** < **AP11** < **AP14** (Figure 2). The onsets of absorption are all red-shifted relative to **RR9** indicating a higher photocurrent is possible in devices based on **AP11**, **AP14**, **AP16**, and **AP17** by conversion of lower energy photons (Table 1). These dyes are designed to be intramolecular charge transfer (ICT) dyes with ether donor groups positioned on one side of the molecule in order to position the highest occupied orbital density on the aryl ether region, which can be transferred to the electron-deficient region. As such, **AP17** is expected to be the least red-shifted in the series, whereas none of the 4 alkoxy groups are in resonance conjugation with the TPD bridge. **AP16** introduces an additional alkoxy group to **AP17**, which is in conjugation with the TPD bridge resulting in a red-shift of the lowest energy absorption curve feature. **AP11** is the next most red-shifted with a single alkoxy group that is in conjugation with the TPD bridge. Finally, the most red-shifted dye is **AP14**. The relative red-shift of **AP14** compared to the other dyes is predictable since **AP14** has the largest number of alkoxy groups (2) in conjugation with the TPD bridge.

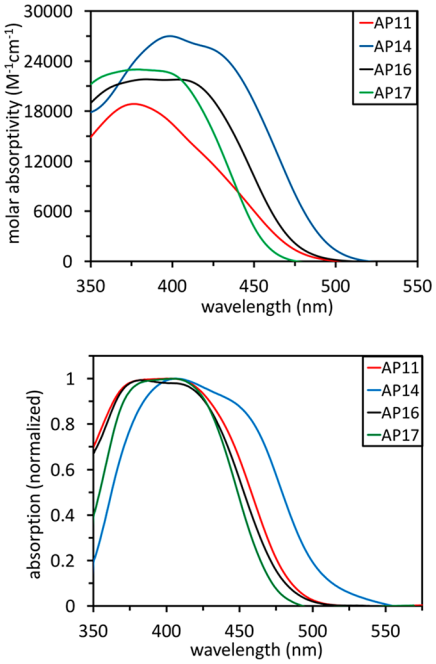

Figure 2. Molar absorptivities of **AP11**, **AP14**, **AP16**, and **AP17** in dichloromethane (top) and as normalized absorption curves on TiO_2(bottom).

The molar absorptivity (ε) was examined for each of the dyes at the highest absorption point of >350 nm (Table 1). The peak absorption (λ_{max}) for each of the dyes fell between 377 and 399 nm with ε values ranging from 19 000 to 27 000 M^{-1} cm^{-1} in the following order: **AP11** < **AP16** ≤ **AP17** < **AP14**. The number of alkyl chains and the strength of the ICT transition are known to affect molar absorptivity.[43,44] **AP11** with the fewest alkyl chains had the lowest molar absorptivity (19 000 M^{-1} cm^{-1}), followed by similar values for **AP16** and **AP17** (22 000−23 000 M^{-1} cm^{-1}) with 5 and 4 alkoxyl chains, respectively. **AP14** has the highest molar absorptivity in the series (27 000 M^{-1} cm^{-1}), which may be due to the donor group of **AP14** having two alkoxy chains in conjugation with the TPD group resulting in a stronger ICT band. On TiO_2 films, the dyes each show similar trends in energy of absorption and curve shapes as in solution except for **AP11** (Figure 2, Table 1). **AP11** shows a change in curve shape on film with the low-energy shoulder at a similar height to the high energy feature, which is different to solution measurements where these features are significantly different heights. The origin of this change in absorption curve feature height on TiO_2 is not apparent for **AP11**; however, aggregative effects are a potential cause as has been observed before.[45−48] This hypothesis is consistent with **AP11** uniquely having only one alkyl chain and no ortho substituted ether groups to reduce π-system planarity. The absorption curve onsets are also shifted by about 50 nm for each dye on TiO_2 compared to solution.

3.3. Electrochemical Properties. Electrochemical analysis for each dye was conducted via differential pulse voltammetry (DPV) in solution or via cyclic voltammetry (CV) on TiO_2-coated FTO (fluorine-doped tin oxide) (Table 1 and Figure 3). **AP11** had the highest value ground state oxidation potential (strongest oxidant as a cation, $E_{(S^+/S)}$) at 1.81 V vs normal hydrogen electrode (NHE) in 1,2-dichloroethane (DCE). A similar value is observed when **AP11** is measured on TiO_2 electrodes (1.85 V). **AP14** has the lowest value $E_{(S^+/S)}$ in solution at 1.52 V and on TiO_2 at 1.73 V. Concerning the shift in oxidation potential at the TiO_2 surface, significant changes in organic dye energetics are commonly empirically observed in literature when solution and TiO_2 films are compared.[32,49,50] **AP16** and **AP17** were at intermediate $E_{(S^+/S)}$ values for this series at 1.62 and 1.61 V, respectively. The oxidation potentials for both dyes increased to 1.95 and 1.85 V on TiO_2, respectively. Notably, as a cation, all of these dyes are adequate energetically to oxidize $Fe(bpy)_3^{2+}$ at 1.37 V vs NHE with a regenerative driving force (ΔG_{reg}) of ≥300 mV on TiO_2 (Figure 3). The cations of the dyes studied herein are significantly stronger oxidizing than typical organic dyes, which

DOI: 10.1021/acsaem.9b00730
ACS Appl. Energy Mater. 2019, 2, 5547−5556

Table 1. Optical and Electrochemical Properties of AP11, AP14, AP16, and AP17 in Solution and on TiO_2 when Listed

	Optical Data (in DCM unless noted)				Electrochemical Data			
dye	λ_{max} (nm)[a]	$E_{(0-0)}$ (eV)[b]	$\lambda_{onset}^{TiO_2}$ (eV)[c]	ε (M^{-1} cm^{-1})	$E_{(S^+/S)}$ (V)[d]	$E_{(S^+/S)}^{TiO_2}$ (V)[e]	$E_{(S^+/S^*)}$ (V)[f]	$E_{(S^+/S^*)}^{TiO2}$ (V)[g]
AP11	377	2.61	2.53	19 000	1.81	1.85	−0.80	−0.68
AP14	399	2.51	2.41	27 000	1.52	1.73	−0.99	−0.89
AP16	384	2.77	2.53	22 000	1.62	1.95	−1.15	−0.91
AP17	379	2.81	2.61	23 000	1.61	1.85	−1.20	−0.76

[a]These are the peak values observed. The **AP** dyes have a red-shifted shoulder relative to this peak (see Figure 2). See Table 2 values and related discussion below for more details. [b]Measured from the intercept of the absorption and emission curves (Figure S14). [c]Onset values are taken from the *x*-intercept of a tangent line on the low-energy side of the absorption curve. Since the absorption curves are broad on TiO_2 λ_{max} values are not reported. [d]Reported from DPV in 1,2-dichloroethane (Figure S8). [e]Reported from cyclic voltammetry as the anodic peak current (E_{pa}) value due to irreversibility (Figure S13). [f]Calculated from the equation $E_{(S^+/S^*)} = E_{(S^+/S)} - E_{(0-0)}$. [g]Calculated from the equation $E_{(S^+/S^*)} = E_{(S^+/S)} - E_g^{opt}$, where $E_g^{opt} = 1240/\lambda_{onset}^{TiO_2}$. See SI for additional optical and electrochemical data analyses using methods directly comparable to **RR9** (Figures S3−S12 and Tables S1−S2).

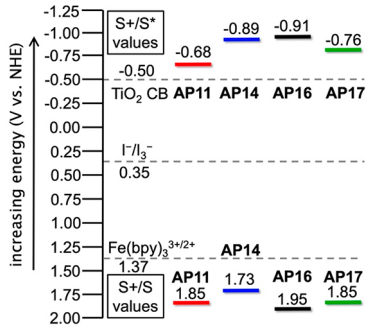

Figure 3. Energy level diagram for **AP11**, **AP14**, **AP16**, and **AP17** on TiO_2. The TiO_2 CB is taken as −0.50 V versus NHE in MeCN as is generally approximated in the field,[53−56] but it should be noted that this value can shift dramatically based on environment.[57−59] The potential of the I^-/I_3^- redox shuttle system is shown as a reference point as a single potential as is generally reported value in the field;[7,8,53,56,60] however, it should be noted that this is a crude approximation and the I_3^-/I^- system is too complex to accurately report as a single number.[61,62]

have $E_{(S^+/S)}$ values near 1.0 V and are not suitable for the efficient oxidation of $Fe(bpy)_3^{2+}$.[8,10,51,52]

Importantly, **AP11**, **AP14**, **AP16**, and **AP17** are all red-shifted and retain more positive oxidation potentials (>1.73 V) relative to **RR9**, which indicates the excited-state energy has diminished for the **AP** series dyes relative to **RR9**. This is desirable since excess excited-state energy is thermal energy waste for applications involving TiO_2, such as HV DSCs. The excited-state oxidation potentials ($E_{(S^+/S^*)}$) for the **AP** series dyes are calculated with the equation $E_{(S^+/S^*)} = E_{(S^+/S)} - E_g^{opt}$, where E_g^{opt} is estimated from the absorption curve onset on TiO_2 (see Table 1 caption). The $E_{(S^+/S^*)}$ values become more negative in the following order: **AP11** > **AP17** > **AP14** > **AP16** on TiO_2 film. The excited-state values shift to less negative values by 100−440 mV on TiO_2 films when compared to solution. The largest changes between solution and film in $E_{(S^+/S^*)}$ values are observed with dyes **AP16** (240 mV change) and **AP17** (440 mV change). The origin for this change in $E_{(S^+/S^*)}$ value when solution and film is compared is not obvious from these studies. The $E_{(S^+/S^*)}$ values on TiO_2 show driving forces for electron injection (ΔG_{inj}) into the TiO_2 conduction band (CB) of 180−410 mV. Thus, the **AP** dye cations are stronger oxidizing than the $\mathbf{RR9}^+$ (1.56 V oxidation potential), and the **AP** series dyes could have less photon conversion energy waste due to the lower excited-states.

3.4. Computational Analysis. Spatial orbital positioning is critical for organic chromophores to function efficiently in photoinduced interfacial electron transfer systems. Ideally, the orbital where the electron originates should be far from the semiconductor surface to slow back electron transfer after charge separation, and the orbital where the electron travels to after photoexcitation should be close to the surface of the semiconductor for efficient electron transfer events. To evaluate the orbitals involved during photoexcitation and the spatial positioning of these orbitals, DFT and TD-DFT calculations were performed at the B3LYP/6-311G(d,p) level for the **AP** series dyes.[63] Upon geometry optimization, TD-DFT was analyzed to identify the key molecular orbitals within these dyes for the first significant low energy transition. For dyes **AP11** and **AP14**, the first state (lowest energy) calculated shows a ≥98% highest occupied molecular orbital (HOMO) to lowest unoccupied molecular orbital (LUMO) transition with strong oscillator strengths of 0.714 and 0.486 observed, respectively. The corresponding vertical transition energy for

Table 2. Computational Data from TD-DFT Analysis of AP11, AP14, AP16, and AP17

dye	transition[a]	contribution (%, state)	vert. trans. (nm)	exp. shoulder (nm)[b]	Δ*E* comp. vs exp. (eV)	oscillator strength
AP11	H → L	99, $S_0 \rightarrow S_1$	466	430	0.22	0.714
AP14	H → L	98, $S_0 \rightarrow S_1$	480	440	0.23	0.486
AP16	H → L	99, $S_0 \rightarrow S_1$	579			0.002
	H-1 → L	99, $S_0 \rightarrow S_2$	533			0.098
	H-2 → L	99, $S_0 \rightarrow S_3$	451	420	0.2	0.674
AP17	H → L	99, $S_0 \rightarrow S_1$	586			0.001
	H-1 → L	99, $S_0 \rightarrow S_2$	525			0.060
	H-2 → L	98, $S_0 \rightarrow S_3$	435	405	0.21	0.820

[a]H = HOMO, H-1 = HOMO−1, H-2 = HOMO−2, L = LUMO. [b]This value is estimated from the lowest energy feature of the absorption curve taken in dichloromethane.

DOI: 10.1021/acsaem.9b00730
ACS Appl. Energy Mater. 2019, 2, 5547−5556

each dye is 466 (**AP11**) and 480 nm (**AP14**), which is closely correlated (within 0.23 eV) to the observed experimental λ_{max} shoulder energy for each dye (Table 2). For both **AP16** and **AP17**, the first two states analyzed had low oscillator strengths (<0.1), and the third state (HOMO−2 → LUMO, ≥98%) is the lowest energy state with a strong oscillator strength (0.674 and 0.820, respectively). The energy of this third state is again in close correlation to the lowest energy experimentally observed absorption curve feature (within 0.21 eV). Having identified the key orbitals involved in the first strong optical transition for each dye, the spatial positioning of these orbitals was analyzed for suitable photoinduced interfacial charge transfer characteristics (Figure 4). The occupied molecular

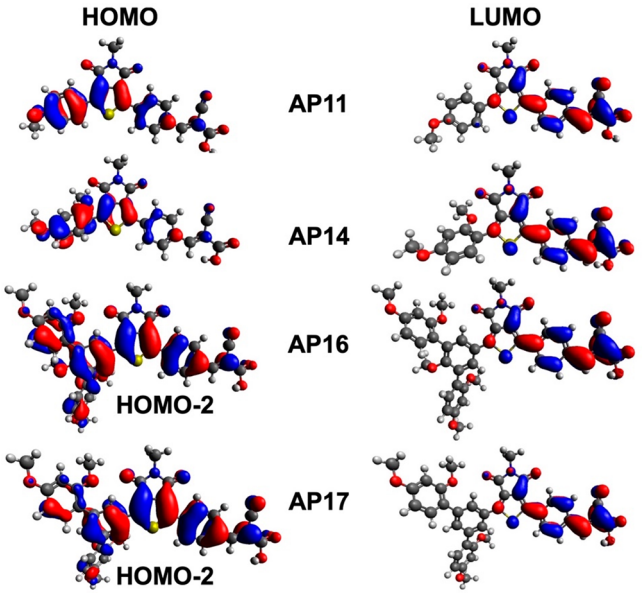

Figure 4. HOMO or HOMO−2 and LUMO orbitals of **AP11**, **AP14**, **AP16**, and **AP17**. The highest energy occupied orbital involved in the lowest energy first major transition ($f \geq 0.1$) is the HOMO−2 orbital for **AP16** and **AP17** (see discussion above).

orbital for each dye (HOMO for **AP11** and **AP14**; HOMO−2 for **AP16** and **AP17**) shows positioning primarily on the benzene ring of the donor region attached to the TPD bridge and onto the TPD bridge. The LUMO for each dye is positioned primarily on the TPD bridge and benzene-cyano acrylic acid groups. These calculations confirm ICT is occurring as the dominate low energy transition for these dyes. The spatial positioning of the orbitals is also ideal for electron injection into TiO_2 and prolonging charge separation.

3.5. High-Voltage DSC Devices. HV DSC devices were fabricated with these dyes with TiO_2 and $Fe(bpy)_3^{3+/2+}$ as a redox shuttle to demonstrate the utility of a strong photoinduced oxidant in an application. The open-circuit voltage (V_{OC}) for the **AP** series dyes was in the range of 1.26−1.32 V. These values are near the high performing **RR9** at 1.42 V (Figure 5, Table 3).[10] The short circuit current density (J_{SC}) improved for all of the **AP** dyes relative to the value reported for **RR9** by up to 25% for a maximum J_{SC} of 3.5 mA/cm^2. This increase is due to the lowering of the **AP** series dye excited-state to narrow the dye optical gap resulting in a red shift of the **AP** series dye incident photon-to-current conversion efficiency (IPCE) onset relative to **RR9** by about 25 nm (Figure 5). **AP11** shows an IPCE peak near 60% with the remaining dyes

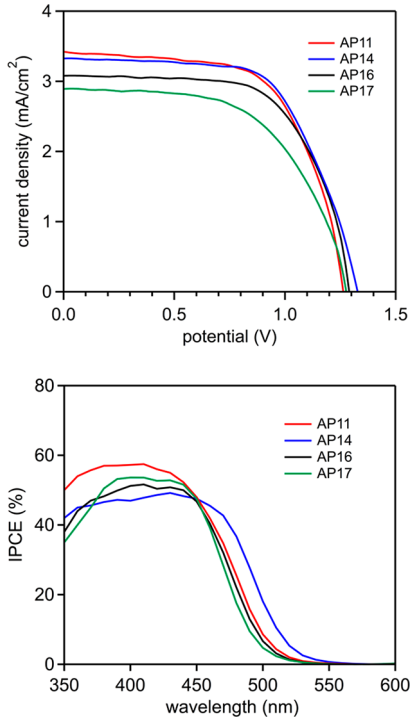

Figure 5. $J-V$ curves (top) and IPCE spectra (bottom) for **AP11**, **AP14**, **AP16**, and **AP17** based DSC devices with $Fe(bpy)_3^{3+/2+}$.

Table 3. Device Data with Dyes AP11, AP14, AP16, and AP17.[a]

dye	V_{oc} (V)	J_{sc} (mA/cm^2)	FF	PCE (%)
AP11	1.26	3.50	0.63	2.9
AP14	1.32	3.40	0.63	2.7
AP16	1.29	3.10	0.65	2.6
AP17	1.27	2.90	0.58	2.2
RR9	1.42	2.80	0.47	1.9

[a]See SI for device fabrication details, device compositions, and integrated photocurrent densities from the IPCE spectrum.

having maximum IPCE values of about 50−55%. The IPCE intensity is controlled by a number of factors concerning both optical properties and charge transport properties of the device, and the reason for the higher IPCE of **AP11** is not obvious in these studies since the dye loading density was similar to **AP14** and **AP17** at 4.1−4.5 × 10^{-7} mol/cm^2 (Table S5). **AP16** shows a modestly diminished dye loading density at 3.1 × 10^{-7} mol/cm^2; however, the IPCE peak intensity is similar to that of **AP14** and **AP17**. All of the IPCE values are likely negatively impacted from the absorbance of the $Fe(bpy)_3^{2+}$ redox shuttle which has a molar absorptivity of 9500 M^{-1} cm^{-1} in MeCN with the absorption onset extending beyond that of the dyes studied here (see Figures S16 and S17 and Table S4 for device data with the I_3^-/I^-, and $Co(bpy)_3^{3+/2+}$ electrolytes). $Fe(bpy)_3^{3+}$ does not have an appreciable absorption in the visible spectral region (Figure S15). Notably, the fill factor (FF) increased to 0.58−0.65 for the **AP** series devices relative to the reported **RR9** device at 0.47. While the origin of this increase is not directly obvious, we do note that the **AP** series dyes shows the appearance of a slight reverse wave via CV measurements while **RR9** shows no signs of a reverse wave indicating a potentially more stable **AP**$^+$ species is formed (Figure S7). According to the equation PCE

DOI: 10.1021/acsaem.9b00730
ACS Appl. Energy Mater. 2019, 2, 5547−5556

= $(V_{OC} \times J_{SC} \times FF)/I_0$, where PCE is power conversion efficiency and I_0 is the sun intensity (set to near 1 sun in these studies as measured with a calibrated reference solar cell), a PCE of 2.2−2.9% is observed for these devices which improves on the 1.9% PCE of the **RR9** device while maintaining comparable photovoltages.

Small modulated photovoltage transient (SMPVT) studies provide a method to analyze electron lifetimes in TiO_2 for DSC devices under continuous illumination at varied light intensities. These studies are often correlated to the rate of recombination of electrons in TiO_2 with the oxidized redox shuttle.[64] Electron lifetimes were found to increase in the following order **AP17** ≅ **AP11** < **AP16** < **AP14** which matches the observed open circuit voltages from current−voltage curve measurements (Figure 6). Recombination is likely fastest with

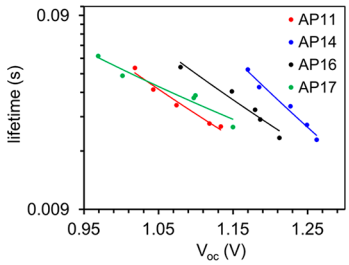

Figure 6. Small modulated photovoltage transient measurements of **AP11**, **AP14**, **AP16**, and **AP17**.

AP11 and **AP16**, while **AP14** limits the rate of recombination the most in this series. The origin of the change in recombination rate is challenging to explicitly determine since the rate of recombination is related to many factors such as dye-redox shuttle noncovalent interactions, surface orientation, surface footprint, solid-state ordering, and dye loading. However, the **AP14** aryl-ether donor group is significantly rotated out of plane with the TPD conjugated system due to an ortho substituted alkyl ether relative to the TPD group. The out of plane alkyl ether substituent near the TPD bridge likely aids in adding a protective insulting group relatively close to the TiO_2 surface when compared with the other **AP** dyes. The out of plane alkyl ether group conveniently provides surface insulation in a separate direction to that of the TPD alkyl group which likely leads to less recombination, and as a result, the highest photovoltage of the series.

4. CONCLUSIONS

Thienopyrroledione is investigated as an electron deficient π-bridge for the photoinduced generation of a strong oxidant at a semiconductor interface with visible light. Through DPV studies in solution and CV studies on TiO_2 films, the oxidizing potential of TPD dye cations is found to be significantly stronger than that of a benzothiadiazole analogue. The UV−vis absorption spectroscopy reveals a modest red-shift of the TPD based dyes as well, which indicates the excited-state has been lowered for the TPD dyes relative to BTD. This is desirable for applications involving TiO_2 to avoid excess photon energy waste during photoinduced electron injection into the TiO_2 CB. Via computational studies, the primary orbitals contributing to photoexcitation were found to be well positioned spatially for photoinduced electron transfer at a metal oxide interface with potentially good charge separation duration. HV DSC devices were fabricated with the **AP** series dyes and compared to record performing **RR9** under identical conditions. The photovoltage from **AP14** was found to be comparable to that of **RR9** (1.32 vs 1.42 V). The **AP14** device was found to have a higher photocurrent and fill factor leading to a higher power conversion efficiency relative to the reported **RR9** device. The range of photovoltages obtained was correlated to the rate at which electrons in TiO_2 recombine with $Fe(bpy)_2^{3+}$ for each of the **AP** series devices with **AP14** showing the slowest recombination and highest photovoltage. Future directions are focused on modifying the donor group to generate stronger photoinduced oxidants and evaluation of additional redox shuttles that can demonstrate the full oxidation strength of the **AP** series dye cations in an application by diminishing thermal energy waste during regeneration.

■ ASSOCIATED CONTENT

Supporting Information

The Supporting Information is available free of charge on the ACS Publications website at DOI: 10.1021/acsaem.9b00730.

Cyclic voltammogram information, additional photovoltaic device characterization information, device fabrication protocols, NMR spectra, and DFT geometry coordinates (PDF)

■ AUTHOR INFORMATION

Corresponding Author

*E-mail: delcamp@olemiss.edu.

ORCID

Roberta R. Rodrigues: 0000-0003-2930-2451
Nathan I. Hammer: 0000-0002-6221-2709
Jared H. Delcamp: 0000-0001-5313-4078

Funding

This research was supported by the U.S. Department of Energy, Office of Science, Office of Basic Energy Sciences, under Award DE-SC0019131, for all studies, except the fluorescence spectroscopy studies performed by A.L.D. and N.I.H., which were supported by NSF OIA-1757220.

Notes

The authors declare no competing financial interest.

■ REFERENCES

(1) Yan, N. F.; Li, G. R.; Gao, X. P. Electroactive Organic Compounds as Anode-Active Materials for Solar Rechargeable Redox Flow Battery in Dual-Phase Electrolytes. *J. Electrochem. Soc.* **2014**, *161*, A736−A741.

(2) Lei, B.; Li, G.-R.; Chen, P.; Gao, X.-P. A Quasi-Solid-State Solar Rechargeable Battery with Polyethylene Oxide Gel Electrolyte. *ACS Appl. Energy Mater.* **2019**, *2*, 1000−1005.

(3) Schmidt, D.; Hager, M. D.; Schubert, U. S. Photo-Rechargeable Electric Energy Storage Systems. *Adv. Energy Mater.* **2016**, *6*, 1500369.

(4) Lhermitte, C.; Sivula, K. Alternative Oxidation Reactions for Solar-driven Fuel Production. *ACS Catal.* **2019**, *9*, 2007−2017.

(5) Yu, Z.; Li, F.; Sun, L. Recent advances in dye-sensitized photoelectrochemical cells for solar hydrogen production based on molecular components. *Energy Environ. Sci.* **2015**, *8*, 760−775.

(6) Sheridan, M. V.; Wang, Y.; Wang, D.; Troian-Gautier, L.; Dares, C. J.; Sherman, B. D.; Meyer, T. J. Light-Driven Water Splitting Mediated by Photogenerated Bromine. *Angew. Chem., Int. Ed.* **2018**, *57*, 3449−3453.

DOI: 10.1021/acsaem.9b00730
ACS Appl. Energy Mater. 2019, 2, 5547−5556

(7) Sun, Z.; Liang, M.; Chen, J. Kinetics of Iodine-Free Redox Shuttles in Dye-Sensitized Solar Cells: Interfacial Recombination and Dye Regeneration. *Acc. Chem. Res.* **2015**, *48*, 1541−1550.
(8) Pashaei, B.; Shahroosvand, H.; Abbasi, P. Transition metal complex redox shuttles for dye-sensitized solar cells. *RSC Adv.* **2015**, *5*, 94814−94848.
(9) Zhang, W.; Wu, Y.; Bahng, H. W.; Cao, Y.; Yi, C.; Saygili, Y.; Luo, J.; Liu, Y.; Kavan, L.; Moser, J.-E.; Hagfeldt, A.; Tian, H.; Zakeeruddin, S. M.; Zhu, W.-H.; Grätzel, M. Comprehensive control of voltage loss enables 11.7% efficient solid-state dye-sensitized solar cells. *Energy Environ. Sci.* **2018**, *11*, 1779−1787.
(10) Rodrigues, R. R.; Cheema, H.; Delcamp, J. H. A High Voltage Molecular Engineered Organic Sensitizer-Iron Redox Shuttle Pair: 1.4 V DSC and 3.3 V SSM-DSC Devices. *Angew. Chem. Int. Ed.* **2018**, *57*, 5472−5476.
(11) Liang, Y.; Wang, Y.; Mu, C.; Wang, S.; Wang, X.; Xu, D.; Sun, L. Achieving High Open-Circuit Voltages up to 1.57 V in Hole-Transport-Material-Free $MAPbBr_3$ Solar Cells with Carbon Electrodes. *Adv. Energy Mater.* **2018**, *8*, 1701159.
(12) Kakiage, K.; Osada, H.; Aoyama, Y.; Yano, T.; Oya, K.; Iwamoto, S.; Fujisawa, J. I.; Hanaya, M. Achievement of over 1.4 V photovoltage in a dye-sensitized solar cell by the application of a silyl-anchor coumarin dye. *Sci. Rep.* **2016**, *6*, 35888.
(13) Marzo, L.; Pagire, S. K.; Reiser, O.; Konig, B. Visible-Light Photocatalysis: Does It Make a Difference in Organic Synthesis? *Angew. Chem. Int. Ed.* **2018**, *57*, 10034−10072.
(14) Prier, C. K.; Rankic, D. A.; MacMillan, D. W. Visible light photoredox catalysis with transition metal complexes: applications in organic synthesis. *Chem. Rev.* **2013**, *113*, 5322−5363.
(15) Koops, S. E.; Barnes, P. R. F.; O'Regan, B. C.; Durrant, J. R. Kinetic Competition in a Coumarin Dye-Sensitized Solar Cell: Injection and RecombinationLimitations upon Device Performance. *J. Phys. Chem. C* **2010**, *114*, 8054−8061.
(16) Heimer, T. A.; Heilweil, E. J.; Bignozzi, C. A.; Meyer, G. J. Electron Injection, Recombination, and Halide Oxidation Dynamics at Dye-Sensitized Metal Oxide Interfaces. *J. Phys. Chem. A* **2000**, *104*, 4256−4262.
(17) Peddapuram, A.; Cheema, H.; Adams, R. E.; Schmehl, R. H.; Delcamp, J. H. A Stable Panchromatic Green Dual Acceptor, Dual Donor Organic Dye for Dye-Sensitized Solar Cells. *J. Phys. Chem. C* **2017**, *121*, 8770−8780.
(18) Ogunsolu, O. O.; Braun, A. J.; Robb, A. J.; Salpage, S. R.; Zhou, Y.; Hanson, K. Influence of Dye-Coordinated Metal Ions on Electron Transfer Dynamics at Dye-Semiconductor Interfaces. *ACS Appl. Energy Mater.* **2019**, *2*, 29−36.
(19) Feldt, S. M.; Lohse, P. W.; Kessler, F.; Nazeeruddin, M. K.; Grätzel, M.; Boschloo, G.; Hagfeldt, A. Regeneration and recombination kinetics in cobalt polypyridine based dye-sensitized solar cells, explained using Marcus theory. *Phys. Chem. Chem. Phys.* **2013**, *15*, 7087−7097.
(20) Saygili, Y.; Stojanovic, M.; Flores-Díaz, N.; Zakeeruddin, S. M.; Vlachopoulos, N.; Grätzel, M.; Hagfeldt, A. Metal Coordination Complexes as Redox Mediators in Regenerative Dye-Sensitized Solar Cells. *Inorganics* **2019**, *7*, 30.
(21) Zhang, X.; Xu, Y.; Giordano, F.; Schreier, M. R.; Pellet, N.; Hu, Y.; Yi, C.; Robertson, N.; Hua, J.; Zakeeruddin, S. M.; Tian, H.; Grätzel, M. Molecular engineering of potent sensitizers for very efficient light harvesting in thin film solid state dye sensitized solar cells. *J. Am. Chem. Soc.* **2016**, *138*, 10742−10745.
(22) Teng, C.; Yang, X.; Li, S.; Cheng, M.; Hagfeldt, A.; Wu, L. Z.; Sun, L. Tuning the HOMO energy levels of organic dyes for dye-sensitized solar cells based on Br-/Br_3- electrolytes. *Chem. - Eur. J.* **2010**, *16*, 13127−13138.
(23) Cheema, H.; Rodrigues, R. R.; Delcamp, J. H. Sequential series multijunction dye-sensitized solar cells (SSM-DSCs): 4.7 V from a single illuminated area. *Energy Environ. Sci.* **2017**, *10*, 1764−1769.
(24) Sherman, B. D.; Bergkamp, J. J.; Brown, C. L.; Moore, A. L.; Gust, D.; Moore, T. A. A tandem dye-sensitized photoelectrochemical cell for light driven hydrogen production. *Energy Environ. Sci.* **2016**, *9*, 1812−1817.
(25) Chae, S. Y.; Park, S. J.; Joo, O. S.; Jun, Y.; Min, B. K.; Hwang, Y. J. Highly stable tandem solar cell monolithically integrating dye-sensitized and CIGS solar cells. *Sci. Rep.* **2016**, *6*, 30868.
(26) Sherman, B. D.; Sheridan, M. V.; Wee, K.-R.; Marquard, S. L.; Wang, D.; Alibabaei, L.; Ashford, D. L.; Meyer, T. J. A Dye-Sensitized Photoelectrochemical Tandem Cell for Light Driven Hydrogen Production from Water. *J. Am. Chem. Soc.* **2016**, *138*, 16745−16753.
(27) Vildanova, M. F.; Nikolskaia, A. B.; Kozlov, S. S.; Shevaleevskiy, O. I. Design and long-term monitoring of DSC/CIGS tandem solar module. *J. Phys.: Conf. Ser.* **2015**, *643*, 012106.
(28) Xiong, D.; Chen, W. Recent progress on tandem structured dye-sensitized solar cells. *Frontiers of Optoelectronics* **2012**, *5*, 371−389.
(29) Ito, S.; Dharmadasa, I. M.; Tolan, G. J.; Roberts, J. S.; Hill, G.; Miura, H.; Yum, J. H.; Pechy, P.; Liska, P.; Comte, P.; Grätzel, M. High-voltage (1.8V) tandem solar cell system using a GaAs/$Al_XGa_{(1-X)}As$ graded solar cell and dye-sensitised solar cells with organic dyes having different absorption spectra. *Sol. Energy* **2011**, *85*, 1220−1225.
(30) Vildanova, M. F.; Nikolskaia, A. B.; Kozlov, S. S.; Shevaleevskiy, O. I.; Larina, L. L. Novel Types of Dye-Sensitized and Perovskite-Based Tandem Solar Cells with a Common Counter Electrode. *Tech. Phys. Lett.* **2018**, *44*, 126−129.
(31) Kroeze, J. E.; Hirata, N.; Koops, S.; Nazeeruddin, M. K.; Schmidt-Mende, L.; Grätzel, M.; Durrant, J. R. Alkyl Chain Barriers for Kinetic Optimization in Dye-Sensitized Solar Cells. *J. Am. Chem. Soc.* **2006**, *128*, 16376−16383.
(32) Ito, S.; Miura, H.; Uchida, S.; Takata, M.; Sumioka, K.; Liska, P.; Comte, P.; Pechy, P.; Gratzel, M. High-conversion-efficiency organic dye-sensitized solar cells with a novel indoline dye. *Chem. Commun.* **2008**, 5194−5196.
(33) Wolfe, R. M.; Reynolds, J. R. Direct Imide Formation from Thiophene Dicarboxylic Acids Gives Expanded Side-Chain Selection in Thienopyrrolediones. *Org. Lett.* **2017**, *19*, 996−999.
(34) Guo, X.; Zhou, N.; Lou, S. J.; Smith, J.; Tice, D. B.; Hennek, J. W.; Ortiz, R. P.; Navarrete, J. T. L.; Li, S.; Strzalka, J.; Chen, L. X.; Chang, R. P. H.; Facchetti, A.; Marks, T. Polymer Solar Cells with Enhanced Fill Factors. *Nat. Photonics* **2013**, *7*, 825−833.
(35) Guo, X.; Ortiz, R. P.; Zheng, Y.; Kim, M. G.; Zhang, S.; Hu, Y.; Lu, G.; Facchetti, A.; Marks, T. J. Thieno[3,4-c]pyrrole-4,6-dione-based polymer semiconductors: toward high-performance, air-stable organic thin-film transistors. *J. Am. Chem. Soc.* **2011**, *133*, 13685−13697.
(36) Feng, Q.; Lu, X.; Zhou, G.; Wang, Z. S. Synthesis and photovoltaic properties of organic sensitizers incorporating a thieno[3,4-c]pyrrole-4,6-dione moiety. *Phys. Chem. Chem. Phys.* **2012**, *14*, 7993−7999.
(37) Ciou, Y. S.; Lin, P. H.; Li, W. M.; Lee, K. M.; Liu, C. Y. Cross-Dehydrogenative Coupling (CDC) as Key-Transformations to Various D-pi-A Organic Dyes: C-H/C-H Synthetic Study Directed toward Dye-Sensitized Solar Cells Applications. *J. Org. Chem.* **2017**, *82*, 3538−3551.
(38) Lu, K.-M.; Li, W.-M.; Lin, P.-Y.; Liu, K.-T.; Liu, C.-Y. Direct C-H Arylation as a Chemoselective Single-Step Access to π-Acceptor-π Type Building Blocks. *Adv. Synth. Catal.* **2017**, *359*, 3805−3817.
(39) Connelly, N. G.; Geiger, W. E. Chemical Redox Agents for Organometallic Chemistry. *Chem. Rev.* **1996**, *96*, 877−910.
(40) Bard, A. J.; Faulkner, L. R. *Electrochemical Methods: Fundamentals and Applications*, 2nd ed.; John Wiley & Sons, Inc.: New York, 2001.
(41) Robitaille, A.; Perea, A.; Bélanger, D.; Leclerc, M. Poly(5-alkyl-thieno[3,4-c]pyrrole-4,6-dione): a study of π-conjugated redox polymers as anode materials in lithium-ion batteries. *J. Mater. Chem. A* **2017**, *5*, 18088−18094.
(42) Shen, Z.; Chen, J.; Li, X.; Li, X.; Zhou, Y.; Yu, Y.; Ding, H.; Li, J.; Zhu, L.; Hua, J. Synthesis and Photovoltaic Properties of Powerful Electron-Donating Indeno[1, 2-b]thiophene-Based Green D-A-π-A

DOI: 10.1021/acsaem.9b00730
ACS Appl. Energy Mater. 2019, 2, 5547−5556

Sensitizers for Dye-Sensitized Solar Cells. *ACS Sustainable Chem. Eng.* **2016**, *4*, 3518−3525.
(43) Yu, Q.-Y.; Liao, J.-Y.; Zhou, S.-M.; Shen, Y.; Liu, J.-M.; Kuang, D.-B.; Su, C.-Y. Effect of Hydrocarbon Chain Length of Disubstituted Triphenyl-amine-Based Organic Dyes on Dye-Sensitized Solar Cells. *J. Phys. Chem. C* **2011**, *115*, 22002−22008.
(44) Huckaba, A. J.; Giordano, F.; McNamara, L. E.; Dreux, K. M.; Hammer, N. I.; Tschumper, G. S.; Zakeeruddin, S. M.; Grätzel, M.; Nazeeruddin, M. K.; Delcamp, J. H. Indolizine-Based Donors as Organic Sensitizer Components for Dye-Sensitized Solar Cells. *Adv. Energy Mater.* **2015**, *5*, 1401629.
(45) Cheema, H.; Baumann, A.; Loya, E. K.; Brogdon, P.; McNamara, L. E.; Carpenter, C. A.; Hammer, N. I.; Mathew, S.; Risko, C.; Delcamp, J. H. Near-Infrared-Absorbing Indolizine-Porphyrin Push-Pull Dye for Dye-Sensitized Solar Cells. *ACS Appl. Mater. Interfaces* **2019**, *11*, 16474−16489.
(46) Delcamp, J. H.; Shi, Y.; Yum, J. H.; Sajoto, T.; Dell'Orto, E.; Barlow, S.; Nazeeruddin, M. K.; Marder, S. R.; Grätzel, M. The Role of π-Bridges in High-Efficiency DSCs Based on Unsymmetrical Squaraines. *Chem. - Eur. J.* **2013**, *19*, 1819−1827.
(47) Zhang, Y.; Cheema, H.; London, A. E.; Morales, A.; Azoulay, J. D.; Delcamp, J. H. Panchromatic cross-conjugated π-bridge NIR dyes for DSCs. *Phys. Chem. Chem. Phys.* **2018**, *20*, 2438−2443.
(48) Mulhern, K. R.; Detty, M. R.; Watson, D. F. Aggregation-Induced Increase of the Quantum Yield of Electron Injection from Chalcogenorhodamine Dyes to TiO_2. *J. Phys. Chem. C* **2011**, *115*, 6010−6018.
(49) Cheema, H.; Peddapuram, A.; Adams, R. E.; McNamara, L. E.; Hunt, L. A.; Le, N.; Watkins, D. L.; Hammer, N. I.; Schmehl, R. H.; Delcamp, J. H. Molecular Engineering of NIR Absorbing Thienopyrazine Double Donor Double Acceptor Organic Dyes for DSCs. *J. Org. Chem.* **2017**, *82*, 12038−12049.
(50) Peddapuram, A.; Cheema, H.; McNamara, L.; Zhang, Y.; Hammer, N.; Delcamp, J. Quinoxaline-Based Dual Donor, Dual Acceptor Organic Dyes for Dye-Sensitized Solar Cells. *Appl. Sci.* **2018**, *8*, 1421.
(51) Hamann, T. W.; Ondersma, J. W. Dye-sensitized solar cell redox shuttles. *Energy Environ. Sci.* **2011**, *4*, 370−381.
(52) Jiang, D.; Darabedian, N.; Ghazarian, S.; Hao, Y.; Zhgamadze, M.; Majaryan, N.; Shen, R.; Zhou, F. Dyes and Redox Couples with Matched Energy Levels: Elimination of the Dye-Regeneration Energy Loss in Dye-Sensitized Solar Cells. *ChemPhysChem* **2015**, *16*, 3385−3388.
(53) Hagfeldt, A.; Boschloo, G.; Sun, L.; Kloo, L.; Pettersson, H. Dye-Sensitized Solar Cells. *Chem. Rev.* **2010**, *110*, 6595−6663.
(54) Urbani, M.; Grätzel, M.; Nazeeruddin, M. K.; Torres, T. Meso-Substituted Porphyrins for Dye-Sensitized Solar Cells. *Chem. Rev.* **2014**, *114*, 12330−12396.
(55) Mishra, A.; Fischer, M. K.; Bauerle, P. Metal-free organic dyes for dye-sensitized solar cells: from structure: property relationships to design rules. *Angew. Chem., Int. Ed.* **2009**, *48*, 2474−99.
(56) Anderson, A. Y.; Barnes, P. R. F.; Durrant, J. R.; O'Regan, B. C. Quantifying Regeneration in Dye-Sensitized Solar Cells. *J. Phys. Chem. C* **2011**, *115*, 2439−2447.
(57) Ronca, E.; Pastore, M.; Belpassi, L.; Tarantelli, F.; De Angelis, F. Influence of the dye molecular structure on the TiO2conduction band in dye-sensitized solar cells: disentangling charge transfer and electrostatic effects. *Energy Environ. Sci.* **2013**, *6*, 183−193.
(58) Raga, S. R.; Barea, E. M.; Fabregat-Santiago, F. Analysis of the Origin of Open Circuit Voltage in Dye Solar Cells. *J. Phys. Chem. Lett.* **2012**, *3*, 1629−1634.
(59) Won, D. I.; Lee, J. S.; Ji, J. M.; Jung, W. J.; Son, H. J.; Pac, C.; Kang, S. O. Highly Robust Hybrid Photocatalyst for Carbon Dioxide Reduction: Tuning and Optimization of Catalytic Activities of Dye/TiO_2/Re(I) Organic-Inorganic Ternary Systems. *J. Am. Chem. Soc.* **2015**, *137*, 13679−13690.
(60) Cole, J. M.; Pepe, G.; Al Bahri, O. K.; Cooper, C. B. Cosensitization in Dye-Sensitized Solar Cells. *Chem. Rev.* **2019**, *119*, 7279−7327.
(61) Boschloo, G.; Hagfeldt, A. Characteristics of the Iodide/Triiodide Redox Mediator in Dye-Sensitized Solar Cells. *Acc. Chem. Res.* **2009**, *42*, 1819−1826.
(62) Ardo, S.; Meyer, G. J. Photodriven Heterogeneous Charge Transfer with Transition-Metal Compounds Anchored to TiO_2 Semiconductor Surfaces. *Chem. Soc. Rev.* **2009**, *38*, 115−164.
(63) Frisch, M. J.; Trucks, G. W.; Schlegel, H. B.; Scuseria, G. E.; Robb, M. A.; Cheeseman, J. R.; Scalmani, G.; Barone, V.; Mennucci, B.; Petersson, G. A.; Nakatsuji, H.; Caricato, M.; Li, X.; Hratchian, H. P.; Izmaylov, A. F.; Bloino, J.; Zheng, G.; Sonnenberg, J. L.; Hada, M.; Ehara, M.; Toyota, K.; Fukuda, R.; Hasegawa, J.; Ishida, M.; Nakajima, T.; Honda, Y.; Kitao, O.; Nakai, H.; Vreven, T.; Montgomery, J. A., Jr.; Peralta, J. E.; Ogliaro, F.; Bearpark, M.; Heyd, J. J.; Brothers, E.; Kudin, K. N.; Staroverov, V. N.; Kobayashi, R.; Normand, J.; Raghavachari, K.; Rendell, A.; Burant, J. C.; Iyengar, S. S.; Tomasi, J.; Cossi, M.; Rega, N.; Millam, J. M.; Klene, M.; Knox, J. E.; Cross, J. B.; Bakken, V.; Adamo, C.; Jaramillo, J.; Gomperts, R.; Stratmann, R. E.; Yazyev, O.; Austin, A. J.; Cammi, R.; Pomelli, C.; Ochterski, J. W.; Martin, R. L.; Morokuma, K.; Zakrzewski, V. G.; Voth, G. A.; Salvador, P.; Dannenberg, J. J.; Dapprich, S.; Daniels, A. D.; Farkas, O.; Foresman, J. B.; Ortiz, J. V.; Cioslowski, J.; Fox, D. J. *Gaussian 09*, revision D.01; Gaussian, Inc.: Wallingford, CT, 2009.
(64) Boschloo, G.; Häggman, L.; Hagfeldt, A. Quantification of the Effect of 4-tert-Butylpyridine Addition to I^-/I_3^-Redox Electrolytes in Dye-Sensitized Nanostructured TiO_2 Solar Cells. *J. Phys. Chem. B* **2006**, *110*, 13144−13150.

DOI: 10.1021/acsaem.9b00730
ACS Appl. Energy Mater. 2019, 2, 5547−5556